# Severe hailstorms near Southern Andes in the presence of mountain waves

A. de la Torre [a],[*], R. Hierro [a], P. Llamedo [a], A. Rolla [a], P. Alexander [b]

[a] Facultad de Ingeniería, Universidad Austral, Avda. J. de Garay 125, C1063ABB Buenos Aires, Argentina
[b] Departamento de Física, FCEN, Universidad de Buenos Aires, Ciudad Universitaria, C1428EGA Buenos Aires, Argentina

## ARTICLE INFO

## ABSTRACT

Experimental satellite and radar data and numerical simulations at constant pressure levels were analyzed to estimate the relative importance of mountain waves during the development of 3 severe deep convection events with abundant hail precipitation in Mendoza, Argentina. The mesoscale numerical simulation model WRF 3.0 was used to determine the regional circulation previous to the deep convection. GPS radio occultation data were used to validate the simulations. It was found that updrafts generated by mountain waves constitute a possible triggering mechanism during the storms initiation. A continuous wavelet transform analysis was applied to the vertical velocity. In all cases, large amplitude stationary waves were observed just before the initiation of convection, possibly triggering it. The horizontal direction of propagation and the corresponding horizontal and vertical wavelengths of both main modes were identified. Vertical velocity and convective inhibition index were found to be potential storm forecasting flags in this region.

© 2011 Elsevier B.V. All rights reserved.

## 1. Introduction

The atmosphere on the lee side of the Andes, enclosed between the subtropical and polar jets, constitutes a well known tropospheric–stratospheric region where high and middle frequency intrinsic mountain waves (MWs) are permanently generated (e.g. Eckermann and Preusse, 1999; de la Torre et al., 2006). In particular, the Mendoza region, roughly situated between latitudes 32 S and 36 S, constitutes by itself a natural laboratory where the recognized main sources of internal gravity waves (GWs) coexist: mountain forcing, geostrophic adjustment, deep convection, frontal activity and shear (e.g. Fritts and Alexander, 2003). A considerable number of deep valleys mainly aligned in a NS direction are a scenario for the development of strong and frequent convection events between late spring and early autumn, sometimes followed by the production of very damaging hail. If the convective instability and moisture flux convergence conditions are appropriate, convection may be triggered by the combination of factors such as upward motion over a frontal zone or diurnal warming and/or orographic lifting (Johns and Doswell, 1992). Moist air masses are then pumped from near the ground to their levels of free convection. The possible influence of orographic forcing in the initiation of deep convection has been suggested in different contexts (e.g. Smith, 1979; Uccellini, 1975). As Doswell (2001) pointed out, mesoscale processes other than those created by deep moist convection can be thought of in several groups: free "internal" instabilities, forced "external" processes, fronts, and GWs. In the case of GWs (Hooke, 1986), occasionally do their amplitudes and size make them obviously important to deep convection. This should take place at low levels, where potentially buoyant parcels exist (Eom, 1975). GW gravity energy tends to leak upward with time, so a waveguide or duct must exist to trap that energy, allowing the wave to retain its amplitude over time and distance. In this case, the horizontal scales of mesoscale convection and of GWs are closely related (Lindzen and Tung, 1976). However, it was observed that the conditions favorable for large-amplitude GWs to propagate for significant time and distance to initiate deep convection are infrequent in the United States (see Hoffman et al., 1995; Koppel et al., 2000).

---

* Corresponding author.
E-mail address: Adelatorre@austral.edu.ar (A. de la Torre).

In the Mendoza region, de la Torre et al. (2004) studied in detail a case registered in summer at mid-latitudes near to the highest Andes Mountains, through a combined analysis of radar, satellite and radiosonde data and numerical simulations. These authors concluded that the deep convection event was generated because of the simultaneous presence of anabatic winds as the triggering mechanism, an accumulation of moist enthalpy and sufficient instability conditions. García-Ortega et al. (2009) analyzed two hailstorm case studies, in which the high diurnal temperatures and the topography of the area favored the formation of thermal mesolows on the lee side of the Andes Range. These authors suggested that the Andes Mountain Range and the solar radiation could have played a key role in triggering convection in the studied zone. Some authors had identified the presence of transient perturbations over the studied region as a possible lifting mechanism to force deep convection events (e.g. Seluchi et
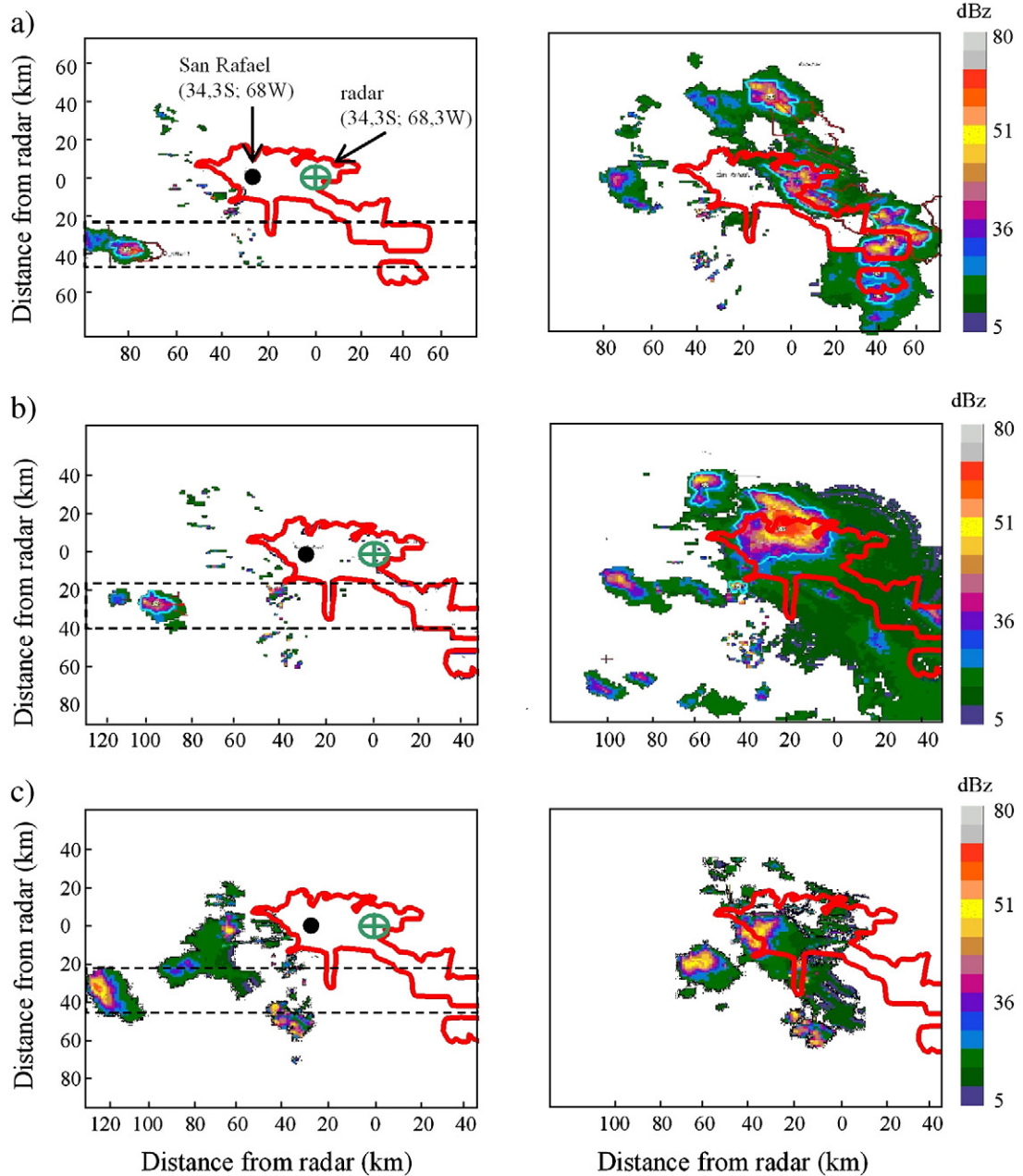


Fig. 1. Refectivity corresponding to the initiation (left) and maximum development (right) of storms a) 1, b) 2 and c) 3. The southern protected oasis is limited in red. The considered 5 zonal $w$ profiles averaged at 600 hPa (see text in Subsection 3.2), adjacent and coincident with the first radar echo, were enclosed between the horizontal dashed lines.
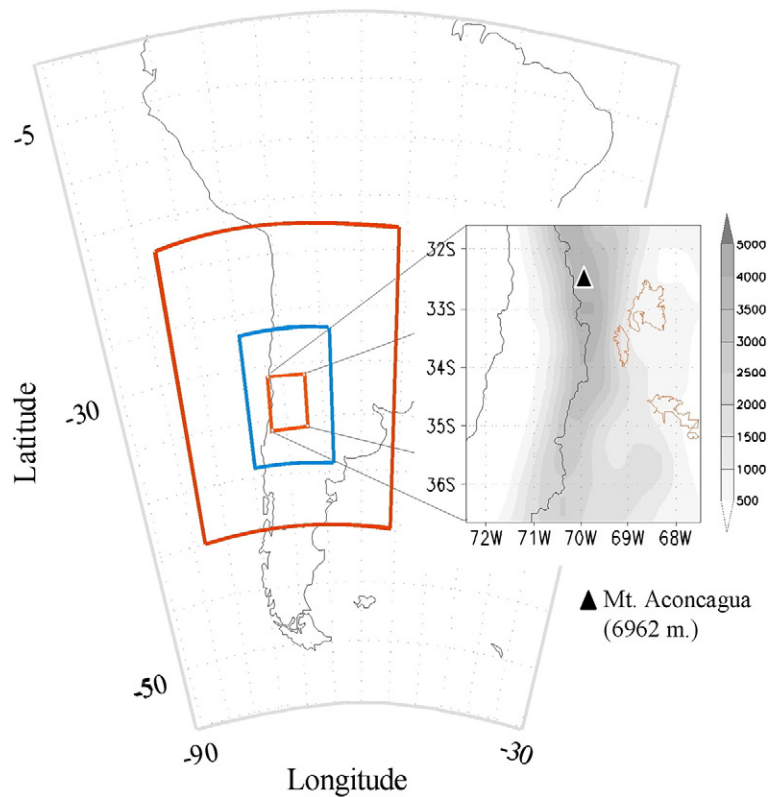
Fig. 2. The three domains selected in the simulations. Topography and the three protected areas in the inner domain.

al., 2006). As far as we know, a detailed discussion of MWs as a possible triggering mechanism for deep convection cases near the Andes has not been proposed yet. Below, we compare three recent case studies in this active GW mid-latitude region near to the locations reported by García-Ortega et al. (2009), registered on 26 Jan 2007, 04 Nov 2006, and 12 Dec 2006, respectively. These storms had a profound economic impact in the studied region, causing

considerable damage to population and vineyards. In particular, the first mentioned case is selected because of its spectacular development, with hailstones larger than tennis balls registered at ground level. This storm affected a total area of around 300 km$^2$. In 70% of it between 80 and 100% of damage was recorded by a hailpad network. Hailpads are used to provide quantitative hailfall measurements and record the time-integrated size distribution and
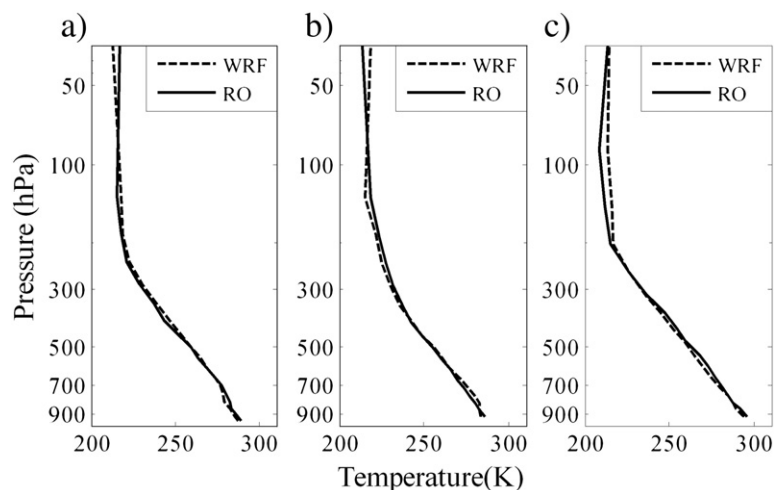


Fig. 3. RO profiles within the 2nd domain retrieved from COSMIC, for validation of cases a) 1, b) 2 and c) 3. Time and average position of the three RO events were: 23Z at (35.5S, 73.7W); 14Z at (34.8S, 73.3W) and 19Z at (34.1S, 64.8W), respectively.

concentration of hailfall. The affected region is currently protected by an operational hail prevention project conducted by the Government of Mendoza (www.contingencias.mendoza.gov.ar). This project includes a three radar network and an operational silver iodide seeding program by aircraft and ground generators.

In Section 2, experimental data from S-band radar and radio occultation (RO) events are described. In Section 3, the

mesoscale numerical simulations conducted for the case study are analyzed. In the last section some conclusions are drawn and an outlook for future research is developed.

## 2. Experimental resources

The initial and maximum reflectivity data during the development of each storm were detected and followed by
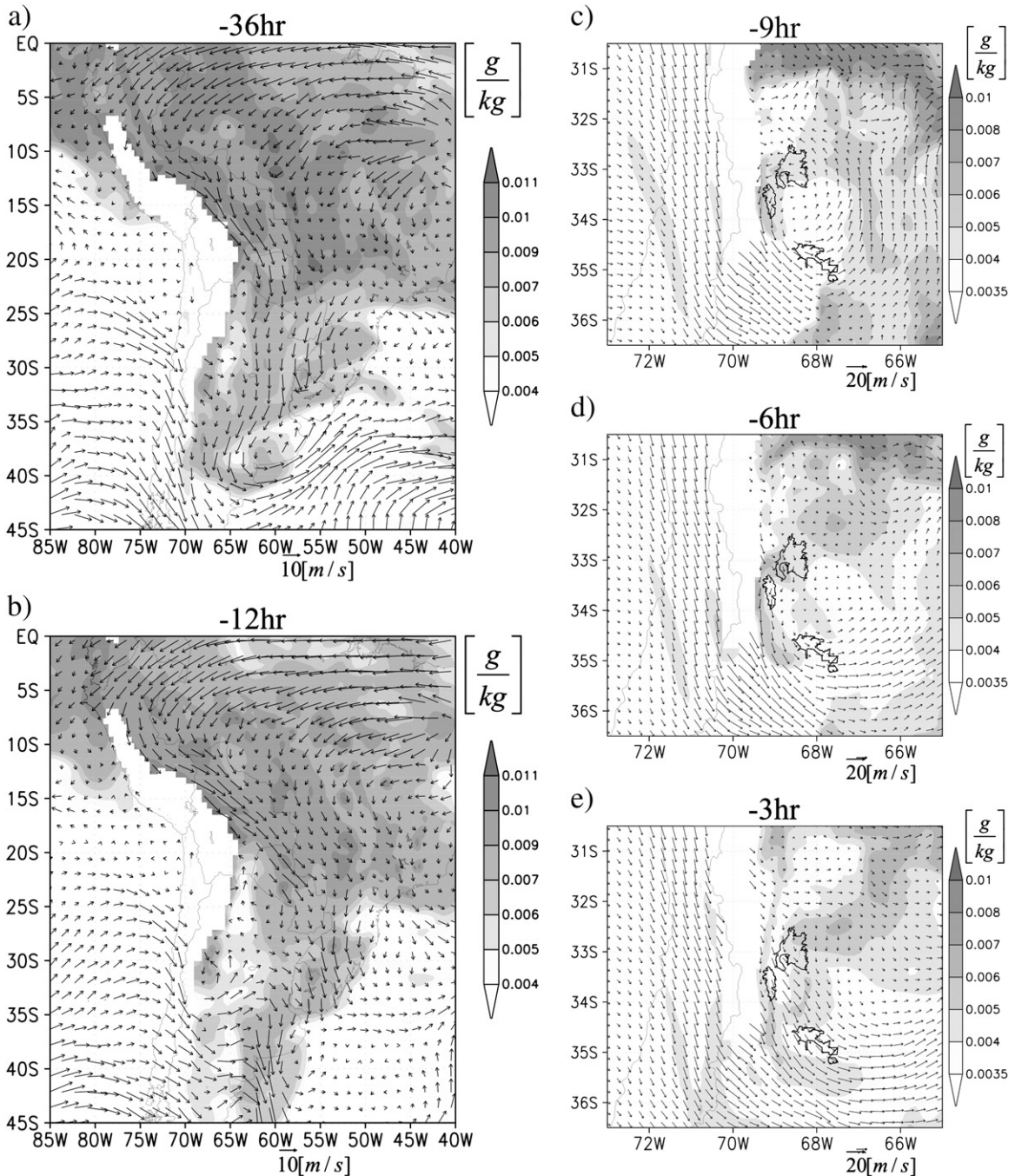


**Fig. 4.** Horizontal flow and mean specific humidity ($q$) averaged between 700 and 850 hPa for case 1, a) 36 and b) 12 h before each event. Same fields, at 12 km horizontal resolution, c) 9, d) 6 and e) 3 h before the deep convection event.

the S-band radar situated near to San Rafael, (Southern Oasis, at 34.6° S and 68.0° W). Radar images are composites selecting the maximum values in overlapping areas. TITAN (Thunderstorm Identification, Tracking, Analysis and Now-casting) radar software provides images of the storms with a spatial resolution of 1 km³. This software identifies storm cells and tracks their evolution (Dixon and Wiener, 1993). In Fig. 1a–c, the reflectivity corresponding to the initiation and maximum development of each storm is shown. The red contour encloses the protected area in the southern oasis. The first echo corresponding to the 3 storms was detected during the early afternoon: case 1, 26 Jan 2007; case 2, 04 Nov 2006;
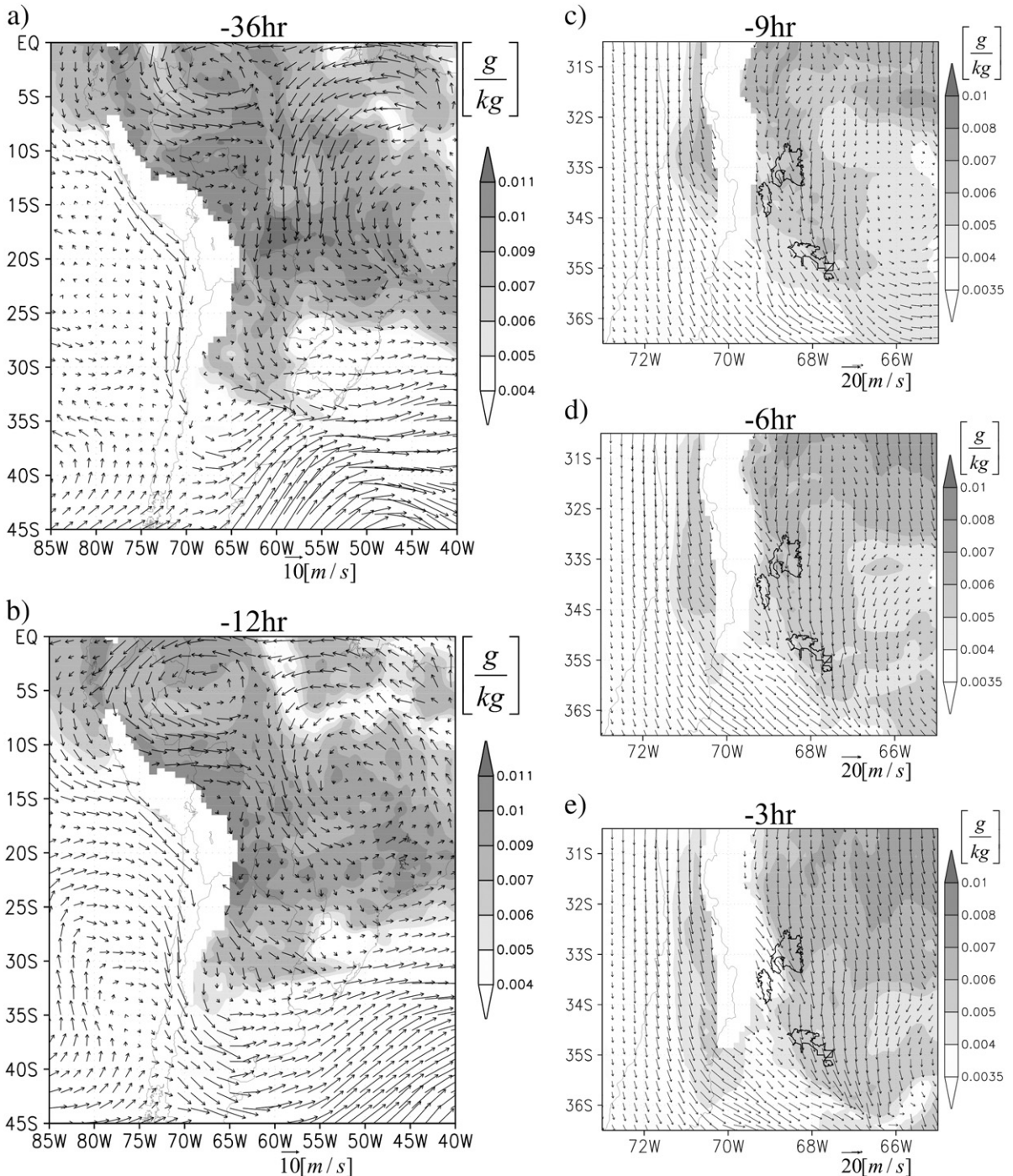


Fig. 5. Same as Fig. 4, for case 2.

and case 3, 12 Dec 2006, at 18:00, 17:00 and 20:00 Z, respectively. LT (Local Time) = Z − 3 h. The storms originated in similar geographic locations, above the so-called area Pampa del Juncalito. They reached their maximum development during their displacement in a SW–NE direction, above the southern oasis.

Temperature *(T)* profiles retrieved during radio occultation (RO) events between GPS (Global Positioning System) and LEO-COSMIC (Low Earth Orbit-Constellation Observing System for Meteorology, Ionosphere and Climate) satellites (Liou et al., 2007) were used to validate the numerical simulations (see Section 3). The COSMIC constellation of six satellites provided
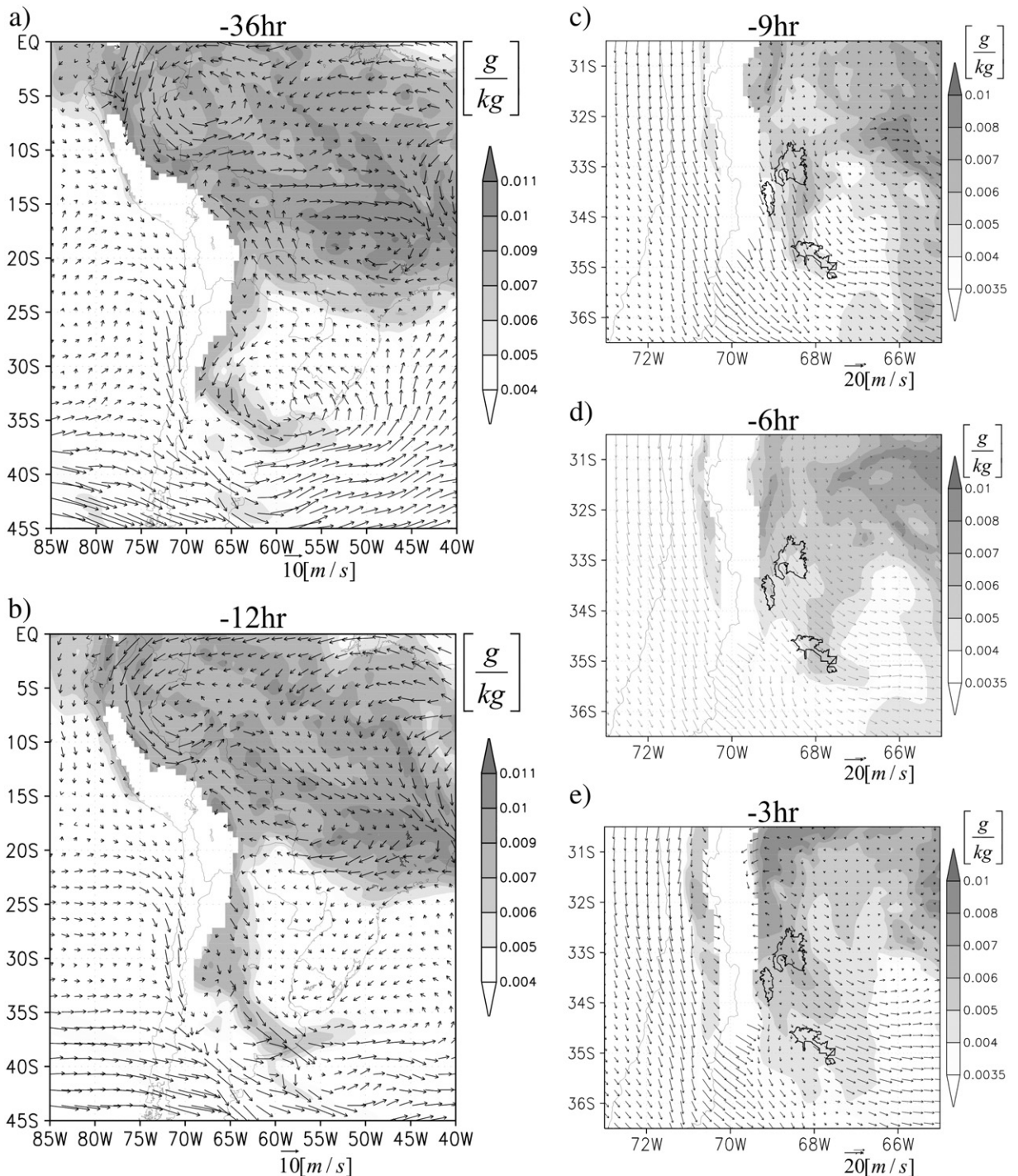


**Fig. 6.** Same as Fig. 4, for case 3.

approximately 1800 RO events per day with an almost global coverage. The GPS RO techniques sensed the atmosphere in the limb mode, providing high vertical resolution $T$ profiles for the troposphere and the stratosphere.

## 3. Numerical simulations

From numerical simulations with the Weather Research and Forecasting (WRF 3.0) regional model (Skamarock et al., 2008), the regional circulation previous to the deep convection events and, in particular, the vertical velocity ($w$) and $T$ fields before and during the development of these events, were determined. The simulations were performed using the $1 \times 1°$ NCEP (National Center of Enviromental Prediction) Global Final Analysis (FNL) to construct initial and boundary conditions. They were carried out in three nested domains over a region containing most of South America, with 43 levels of vertical resolution and a 24 s time step for the highest resolution domain. Soil parameters use the same NCEP FNL. The three domains selected have horizontal resolutions of 36 km ($2500 \times 2500$ km extent), 12 km ($1044 \times 1080$ km extent) and 4 km ($456 \times 564$ km extent) respectively, covering areas with vertices from (83W, 18S) to (56W, 45S), (75W, 39S) to (64W, 27S) and (72W, 36S) to (67W, 31S) (inner domain) (Fig. 2).

For the three domains, the microphysical schemes used were the following: WRF Single Moment-6 class (WSM6; Hong et al., 2004); Yonsei University PBL (YSU; Hong et al., 2006) to represent the planetary boundary-layer physics; Rapid Radiative Transfer Model Longwave (RRTM; Mlawer et al., 1997) and MM5 Dudhia Shortwave (Dudhia scheme; Dudhia, 1989) for radiation processes; the Noah land-surface model (developed jointly by NCAR and NCEP; Skamarock et al., 2008) and Monin–Obukhov scheme; (Monin and Obukhov, 1954) for surface physics and thermal diffusion processes respectively. The cumulus parameterization used was the New Grell scheme (Grell 3; (Grell and Devenyi, 2002)) for the first and second domains while no-cumulus parameterization was selected for the inner domain. The synoptic and regional circulation fields were obtained using the same FNL data running the model in a unique domain under a Lambert conformal map projection, with 27 vertical levels and 64 km horizontal resolution within a coverage area with vertices in (106W, 30N) to (22W, 54S). The parameterizations employed were the same as in the outer domain of the three nested ones, taking output data every 6 h. Based on several tests, the spin up is considered to be 36 h for the 3 nested domain and 48 h for the regional domain.

To validate the simulations, available $T$ RO profiles were used for the 3 cases considered (Fig. 3a–c respectively). The individual data points generated a so-called line of tangent points (LTP). The upper and lower limits (around 40 km height and ground level) of the LTP were separated up to 100 km in the horizontal direction, thus resulting in an atmospheric sounded region different from the vertical direction. The dashed lines represent the WRF $T$ simulation, interpolated along the corresponding LTPs. In the 3 cases, 50 pairs of points were considered and the calculated linear correlation coefficient was always greater than 0.99. The

probability that these high correlation coefficients was a by-product of chance (Hypothesis Test performed) was lower than 0.0001.

### 3.1. Regional circulation

Figs. 4, 5 and 6 show, with a resolution of 36 km, the 700 hPa flow. The specific humidity ($q$) is represented by the low level mean specific humidity (LLMq), which was obtained averaging $q$ between 700 and 850 hPa, 36 and 12 h before each event ($-36$ h and $-12$ h). The same fields, but with a 12 km horizontal resolution, 9, 6 and 3 h before each event are shown ($-9$ h, $-6$ h and $-3$ h, respectively).

Case 1 (Fig. 4) shows a flow arriving from the North of Argentina to the central zone, transporting moist air from tropical latitudes. This low level circulation was interrupted by a SW flow located to the east, 12 h before the storm, allowing the northern flow to penetrate the hold central region of Argentina at this time. Fig. 4c–e depict the increasing LLMq between $-9$ h and $-3$ h while a northerly
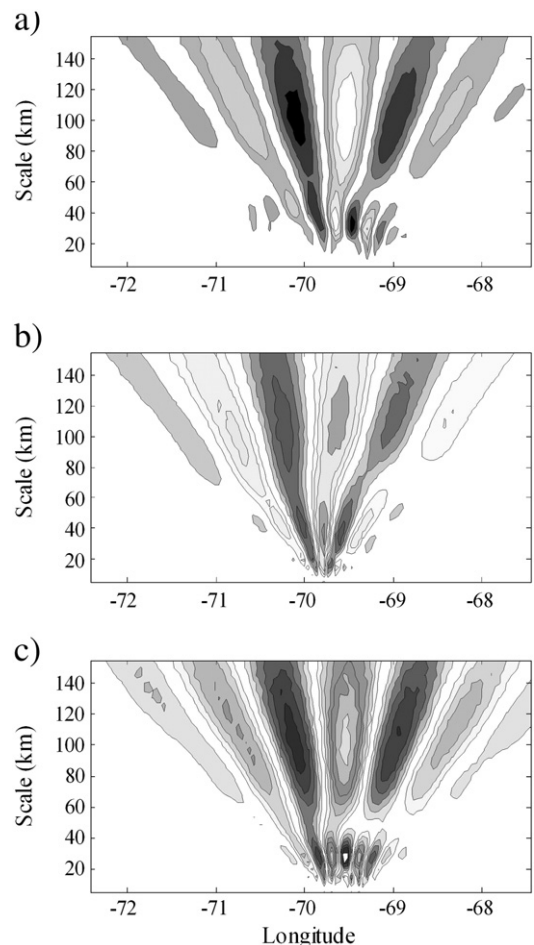
**Fig. 7.** a–c) Morlet CWT for w'$_{bp}$ ZP at 600 hPa, 3 hr before the initiation of storms in cases 1, 2 and 3, respectively.

flow at 700 hPa was present at the East of the mountains, covering the whole area during this 6 h.

In Case 2 (Fig. 5), the −36 h and −12 h fields show that there was an important humidity contribution during the whole period, as well as a northerly predominant component in the wind field along northern and central Argentina. Despite the fact that the low level flow North of 20S was not following a southward direction, the LLMq was apparently transported by a northern current over central and northern Argentina. This current was probably associated to the west branch of the South Atlantic anticyclon, which penetrated the continent over SE of Brazil, entering Argentina from the North and carrying this moist air from the ocean. The 12 km resolution fields show that during 6 h, the presence of LLMq was important over the study region. In time, this variable spread to the South while a persistent low level flow from NW was present.

In case 3 (Fig. 6), 36 h before the event a northerly low level flow covering north and central Argentina carried LLMq from low latitudes to the study region. This circulation, probably associated to a low level jet, was pulled to the North by a SW flow, acquiring a NW–SE orientation and getting the most common position of the South American Low Level Jet (SALLJ) (Saulo et al., 2000). Despite this southern wind, the LLMq was still present over central Argentina 12 h before the event. Fig. 6c–e shows a more detailed LLMq over the study region. It is possible to note the increasing values of LLMq over the southern oasis between −9 h and −3 h.

### 3.2. GW wavelet analysis

Due to the 3D nature of GW signatures, any wave analysis may be conducted along vertical, horizontal or slanted direction. In our case, due to the characteristics of the region under study, with expected dominant high and moderate intrinsic frequency modes, we observed latitude bands at standard pressure levels, between the ground and the tropopause. The horizontal 4 km resolution available at the inner domain of our simulations was sufficient for typical horizontal wavelengths longer than $\lambda_h = 40$ km, according to previous analyses in the region (de la Torre et al., 2006). An important capability of continuous wavelet analysis (CWT) is the identification and localization of main GW modes. In the region considered, these main modes
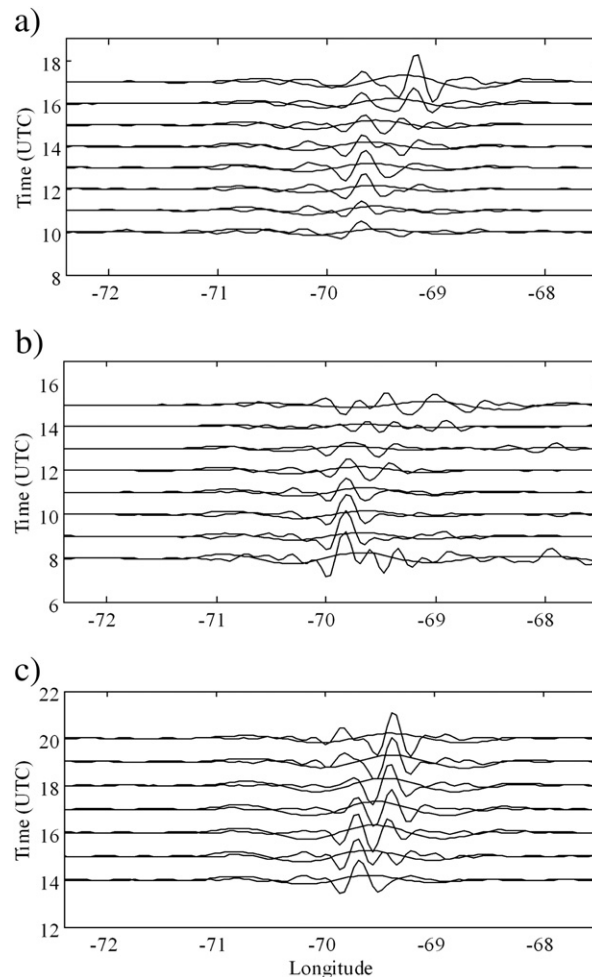


**Fig. 8.** Zonal and time variability of $w'_{bp(40)}$ and $w'_{bp(125)}$ at 600 hPa before and during the deep convection, for cases a) 1, b) 2 and c) 3.

were expected to be observed near to the mountains. Both observations and numerical simulations referred to a ground inertial frame. Then $\lambda_h$ corresponding to each dominant mode was usually conserved throughout the troposphere and was not affected by refractions due to background horizontal wind variation. This was not the case for vertical wavelengths $\lambda_v$.

$w$ constitutes an appropriate dynamical variable to evidence the presence of MWs (e.g. Smith, 1979; Shutts et al., 1988). To isolate the dominant GW modes, we proceeded in each case as follows: we considered 5 zonal profiles at 600 hPa, adjacent and coincident with the first radar echo. These were enclosed between the two horizontal dashed lines in Fig. 1a–c, situated in the 3 cases to the SE of Mount Aconcagua, as shown in Fig. 2. Their average consisted in a 114 data zonal profile (ZP), spaced in each inner 3rd domain at 4 km. A highpass filter with cutoff at 360 km was applied to $w$ and $T$. Subtracting filtered from not filtered ZPs, we obtained $w'$ and $T'$. The filter was applied again with cutoff at 16 km, thus

obtaining band-pass filtered $w'_{bp}$ and $T'_{bp}$ ZPs, retaining GW modes with 16 $\lambda_h$ < 360 km. To separate and locate the dominant spectral components, a CWT was applied. In Fig. 7a–c, the resulting Morlet CWT for $w'_{bp}$ ZP, 3 h before the initiation of each storm is shown. Two clear enhancements corresponding to wave signatures peaking at $k_h = 2\pi/\lambda_h \sim 0.157$ and $0.050$ rad km$^{-1}$ ($\lambda_h = 40$ and 125 km respectively) may be observed in case 1. In cases 2 and 3, similar amplitudes and wavelengths were observed. Mexican hat and Gauss wavelets were tested too, with very similar results (not shown). We re-calculate $w'_{bp}$ from $w'$ with appropriate cutoffs to isolate these two dominant modes, obtaining $w'_{bp(40)}$ and $w'_{bp(125)}$.

In Fig. 8a–c, the zonal variability of $w'_{bp(40)}$ and $w'_{bp(125)}$ at 600 hPa before and during the deep convection, for cases 1, 2 and 3 is shown. The time evolution of these modes evidenced their large amplitude and stationary nature, as expected for MWs. The polarization relations between $T'_{bp(40/125)}$ and $w'_{bp(40/125)}$ revealed predominant $\pi/2$ phase shifts as expected for high frequency MW modes (not shown). These
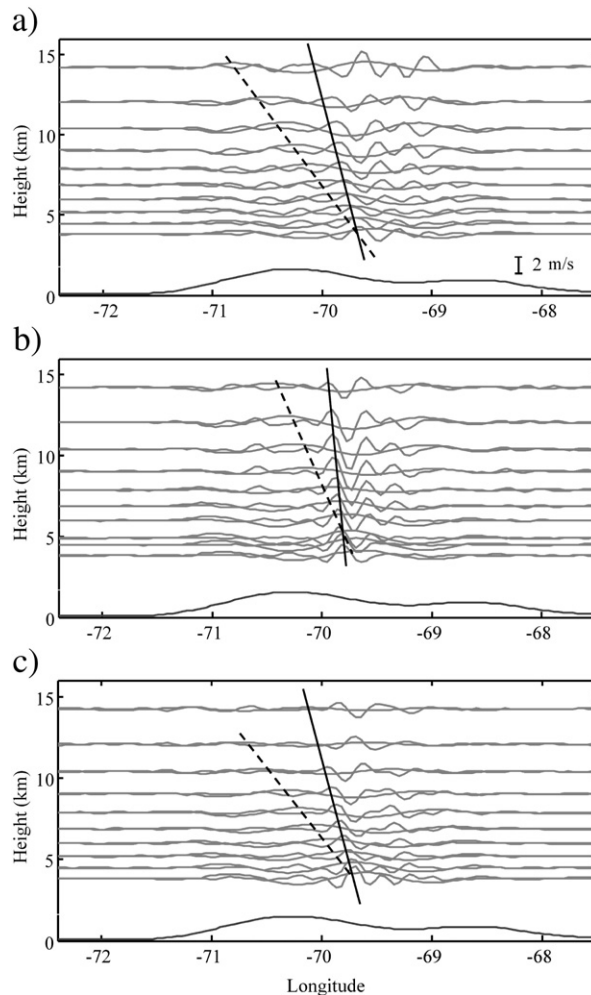


**Fig. 9.** Zonal and time variability of $w'_{bp(40)}$ and $w'_{bp(125)}$ at 600 hPa 3 hr before the initiation of convection, for cases a) 1, b) 2 and c) 3. The lower curve represents the topographic top.

were forced by the Andes Range during several hours until the initiation of deep convection. After this, the large amplitude MWs exhibited smaller amplitudes. In Fig. 9a–c, these two main MW modes, for cases 1, 2 and 3, with westward tilting and $\lambda_v \sim 9$–10 km were observed, respectively, 3 h before the initiation of convection. The lower curve represents the topographic top.

The horizontal direction of propagation for each mode in case 1 (not necessarily the zonal direction) was identified in the following way: centered at the first echo position, radial directions different from zonal were considered, by interpolating the $w'$ numerical data along them (Fig. 10h). In Fig. 10a–g, the corresponding CWTs are shown, for successive $\alpha$ angles relative to the positive zonal direction beginning at $+20°$ and decreasing each 10° intervals until $-40°$. The true horizontal wave vector propagation should be parallel to the direction in which $|k_h|/\lambda_h$ is maximum/minimum. It may be observed that the scales corresponding to the centroids of both modes decreased monotonically with decreasing $\alpha$, reaching minimum values (for both modes) between $-10$ and $-20°$. For even lower values, the scales increased again.

This procedure allowed the estimation of horizontal propagation directions from horizontal soundings or numerical data. Zonal $k_x$ thus obtained for both modes and storm 1 were: $0.157/\cos(\alpha) = 0.162$ and $0.050/\cos(\alpha) = 0.052$ km$^{-1}$. $k_h$ directions thus obtained should lie within the cone enclosed by $-10$ and $-20°$ in Fig. 10h.

Up to this point, we have described the GW parameters and features observed previously and during the 3 storms. From an energetic point of view, additional arguments were needed to support the hypothesis of a mechanical triggering of deep convection by MWs. The convective Available Potential Energy (CAPE) represents the buoyancy available to rising air parcels and describes the instability of the lower atmosphere (e.g. Emanuel, 1994):

$$\text{CAPE} = \int_{\text{LFC}}^{\text{NBL}} g \cdot \frac{T_{v(\text{par})} - T_{v(\text{env})}}{T_{v(\text{env})}} dz, \tag{1}$$

where LFC, NBL and $T_{v(\text{par/env})}$ are the level of free convection, the neutral buoyancy level and the virtual temperature of the selected parcel and environment, respectively.
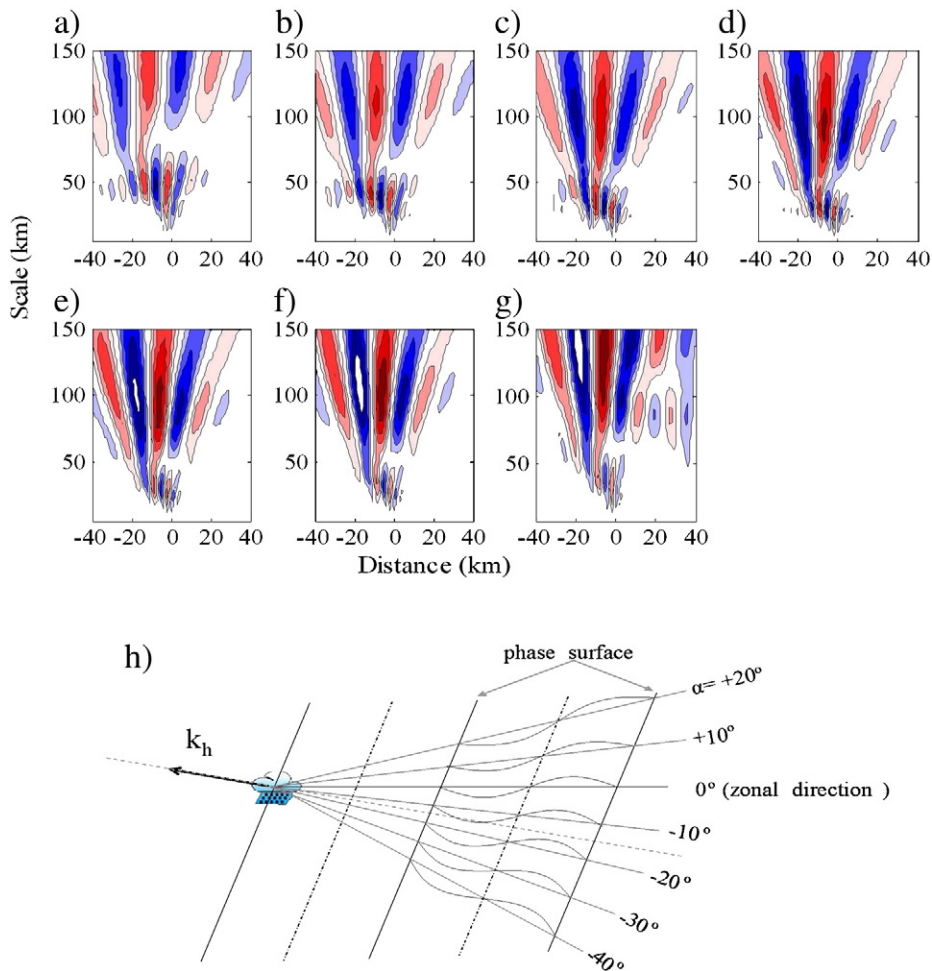


**Fig. 10.** a–g) CWTs for $w'_{bp}$ at successive $\alpha$ angles relative to the zonal direction, beginning at a) $+20°$ and b) to g) respectively decreasing each 10° intervals until $-40°$. h) The selected directions are centered at the first echo position. Along them, $w'$ simulations were previously interpolated.
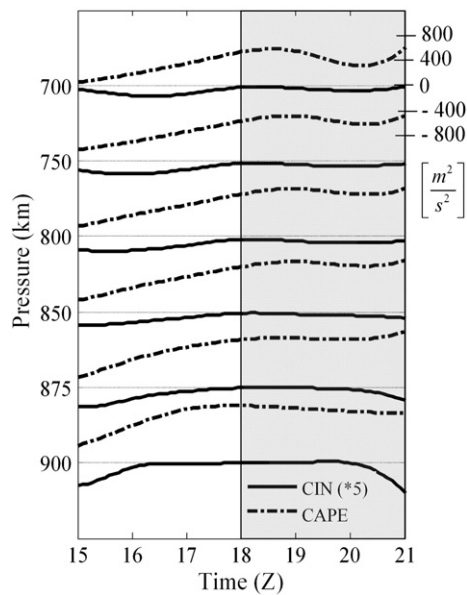
**Fig. 11.** Time variability of CAPE and CIN for initial parcels between 900 and 700 hPa, before and during (light gray) storm development in case 1.

Convective Inhibition (CIN), on the other hand, describes a stable surface layer, which rising air parcels have to overcome to reach the unstable layer. CIN may be derived from the conservation of virtual potential temperature and pseudoequivalent potential temperature, considering different initial parcels and their associated lifting condensation levels and levels of free convection. Following CAPE definition:

$$CIN = \int_{ILL}^{LFC} g \frac{T_{v(par)} - T_{v(env)}}{T_{v(env)}} dz \qquad (2)$$

Here ILL represents an initial lower level for the selected parcel. It is well known (e.g. Riemann-Campe et al., 2009) that high CAPE values do not necessarily lead to strong convection. The simulated air parcel still needs to overcome the stable layer between low levels and the level of free convection. The intensity of this stable layer is quantified by CIN, which is usually a negative quantity. $-$CIN describes a limiting or threshold factor capable of preventing convection despite the existence of very high CAPE values. As an example, in case 1 we estimated CIN and CAPE as a function of time, for initial parcels between 900 and 700 hPa (Fig. 11). We compared the absolute value of CIN with the maximum vertical kinetic energy per unit mass exhibited by the MWs described above, $(w'_{bp})^2/2$. This parameter reached values above $2 \, (m/s)^2$ before the convection initiation, in the three cases. According to this, the mechanical forcing solely provided by MWs would be able to supply the necessary energy to overcome |CIN| values at the region where the storm first developed. Nevertheless, the action of complementary triggering factors, as valley winds, should not be discarded.

## 4. Conclusions

Experimental satellite and radar data and numerical simulations at constant pressure levels were analyzed to estimate the relative importance of MWs during the development of three severe deep convection events with abundant hail precipitation (up to 80–100% of damage per unit area, recorded by a hailpad network) in Mendoza, Argentina. WRF 3.0 model simulations with an inner 4 km resolution domain revealed in the 3 cases the presence of 2 main modes of oscillation with large amplitude and high intrinsic frequency. Their stationary nature was evident at lower altitudes. In all cases, the location and time of the onset of deep convection was well reproduced in the numerical data. In the 3 storms considered in this analysis, MWs were observed just before the initiation of convection. Low level $w'$ and CIN suggest that i) the available energy of MWs was enough to trigger deep convection and ii) these parameters may be considered as potential hailstorm forecasting flags, in comparison with CAPE and other tested instability indexes in this region. After the onset of deep convection, the simulations revealed an irradiation of high frequency GWs downstream the updraft location. A systematic analysis of large amplitude MWs and CIN during the development of a considerable number of severe storms recorded in recent years is being conducted.

## Acknowledgments

## References

de la Torre, A., Vincent, D., Tailleaux, R., Teitelbaum, H., 2004. A deep convection event above the Tunuyán Valley near to the Andes Mountains. Mon. Weather Rev. 132 (9), 2259–2268.

de la Torre, A., Alexander, P., Llamedo, P., Menéndez, C., Schmidt, T., Wickert, J., 2006. Gravity waves above the Andes detected from GPS radio occultation temperature profiles: jet mechanism? Geophys. Res. Lett. 33, L24810. doi:10.1029/2006GL027343.

Dixon, M., Wiener, G., 1993. TITAN: Thunderstorm Identification, Tracking, Analysis and Nowcasting, a radar-based methodology. J. Atmos. Oceanic Technol. 10, 785–797.

Doswell, C.A., 2001. Severe convective storms — an overview. Am. Met. Soc. Meteorol. Monogr. 28 (50), 1–26.

Dudhia, J., 1989. Numerical study of convection observed during the Winter Monsoon Experiment using a mesoscale two-dimensional model. J. Atmos. Sci. 46, 3077–3107.

Eckermann, S.D., Preusse, P., 1999. Global measurements of stratospheric mountain waves from space. Science 286, 1534–1537.

Emanuel, K.A., 1994. Atmospheric Convection. Oxford University Press, New York. 580 pp.

Eom, J., 1975. Analysis of the internal gravity wave occurrence of April 19, 1970 in the Midwest. Mon. Weather Rev. 103, 217–226.

Fritts, D.C., Alexander, M.J., 2003. Gravity wave dynamics and effects in the middle atmosphere. Rev. Geophys. 41, 1003. doi:10.1029/2001RG000106.

García-Ortega, E., López, L., Sánchez, J.L., 2009. Diagnosis and sensitivity study of two severe storm events in the Southeastern Andes. Atmos. Res. 93, 161–178.

Grell, G.A., Devenyi, D., 2002. A generalized approach to parameterizing convection combining ensemble and data assimilation techniques. Geophys. Res. Lett. 29. doi:10.1029/2002GL015311.

Hoffman, E.G., Bosart, L.F., Keyser, D., 1995. Large-amplitude inertia–gravity wave environments: vertical structure and evolution. Preprints, 15th Conf. Wea. Analysis and Forecasting, Norfolk, VA, Amer. Meteor. Soc, pp. 245–248.

Hong, S.-Y., Dudhia, J., Chen, S.-H., 2004. A revised approach to ice microphysical processes for the bulk parameterization of cloud and precipitation. Mon. Weather Rev. 132, 103–120.

Hong, S.-Y., Noh, Y., Dudhia, J., 2006. A new vertical diffusion package with an explicit treatment of entrainment processes. Mon. Weather Rev. 134, 2318–2341.

Hooke, W.H., 1986. Gravity waves. Mesoscale Meteorology and Forecasting: In: Ray, P. (Ed.), Amer. Meteor. Soc. , pp. 272–288.

Johns, R.H., Doswell III, C.A., 1992. Severe local storms forecasting. Weather Forecasting 7, 588–612.

Koppel, L.L., Bosart, L.F., Keyser, D., 2000. A 25-yr climatology of large-amplitude hourly surface pressure changes over the conterminous United States. Mon. Weather Rev. 128, 51–68.

Lindzen, R.S., Tung, K.K., 1976. Banded convective activity and ducted gravity waves. Mon. Weather Rev. 104, 1602–1617.

Liou, Y.-A., Pavelyev, A.G., Liu, S.F., Pavelyev, A.A., Yen, N., Huang, C.Y., Fong, C.J., 2007. FORMOSAT-3 GPS radio mission: preliminary results. IEEE Trans. Geosci. Remote Sens. 45, 3813–3826.

Mlawer, E.J., Taubman, S.J., Brown, P.D., Iacono, M.J., Clough, S.A., 1997. Radiative transfer for inhomogeneous atmosphere: RRTM, a validated correlated-k model for the long-wave. J. Geophys. Res. 102 (D14), 16663–16682.

Monin, A.S., Obukhov, A.M., 1954. Basic laws of turbulent mixing in the surface layer of the atmosphere. Trans. Geophys. Inst. Akad. Nauk. USSR 151, 163–187.

Riemann-Campe, K., Fraedrich, K., Lunkeit, F., 2009. Global Climatology of Convective Available Potential Energy (CAPE) and Convective Inhibition (CIN) in ERA-40 reanalysis. Atmos. Res. 93, 534–545.

Saulo, C., Nicolini, M., Chou, S.C., 2000. Model characterization of the South American low-level flow during 1997–1998 spring–summer season. Climate Dyn. 16, 867–881.

Seluchi, M.E., Garreaud, R.D., Norte, F.A., Saulo, A.C., 2006. Influence of the subtropical Andes on baroclinic disturbances: a cold front case study. Mon. Weather Rev. 134, 3317–3335.

Shutts, G.J., Kitchen, M., Hoare, P.H., 1988. A large amplitude gravity wave in the lower stratosphere detected by radiosonde. Q. J. R. Meteorolog. Soc. 114, 579–594.

Skamarock, W.C., Klemp, J.B., Dudhia, J., Gill, D.O., Barker, D.M., Duda, M., Huang, X.-Y., Wang, W., Powers, J.G., 2008. A Description of the Advaced Research WRF Version 3, NCAR Technical Note NCAR/TN-475 + STR.

Smith, R.B., 1979. The influence of mountains on the atmosphere. Adv. Geophys. 21, 87–230.

Uccellini, L.W., 1975. A case study of apparent graviy wave initiation of severe convective storms. Mon. Weather Rev. 103, 497–513.